Effect of Inherent Damping of the Series Elastic Element on Rendering Performance and Passivity of Interaction Control

Kenanoglu, Celal Umut; Patoglu, Volkan

DOI
10.1115/1.4068463

Publication date
2025

Document Version
Final published version

Published in
Journal of Dynamic Systems, Measurement and Control

ASME Journal of Dynamic Systems, Measurement, and Control
Online journal at:
https://asmedigitalcollection.asme.org/dynamicsystems

Effect of Inherent Damping of the Series Elastic Element on Rendering Performance and Passivity of Interaction Control

Celal Umut Kenanoglu
Department of Cognitive Robotics,
Delft University of Technology,
Delft 2628 CD, The Netherlands
e-mail: umut.kenanoglu@sabanciuniv.edu

Volkan Patoglu[1]
Mechatronics Engineering,
Faculty of Engineering and Natural Sciences,
Sabanci University,
Istanbul 34956, Turkiye
e-mail: volkan.patoglu@sabanciuniv.edu

We study a realistic model of series elastic actuation (SEA) under velocity-sourced impedance control (VSIC), where the inherent damping of the series elastic element is considered during the analysis, even when only the elasticity of the series damped elastic element is used to estimate the interaction forces. We establish a fundamental rendering limitation when the viscous damping of the physical filter is considered in the plant model and prove that passive rendering of stiffness levels that are higher than the stiffness of the physical filter, as well as passive rendering of Voigt models whose damping levels exceed the physical damping of the plant, are possible. We introduce passive physical equivalents of the closed-loop SEA systems with inherent series damping while rendering Kelvin-Voigt, spring, and null impedance models to provide an intuitive understanding of the passivity bounds and to enable rigorous comparisons of rendering performance among various closed-loop systems with different plant models (including or omitting the series damping) and/or controllers (utilizing different interaction force estimates). We present a comprehensive set of experiments to verify our results and demonstrate the effect of including/omitting the damping of the physical filter in the model of SEA. [DOI: 10.1115/1.4068463]

Keywords: physical human–robot interaction, interaction control, series elastic actuation, haptic rendering, fundamental limits of performance, Cauchy's residue theorem, physical realizations, coupled stability, effective impedance

1 Introduction

Series elastic actuation (SEA) is an interaction control paradigm that can provide safe and natural interactions with high stability robustness, and rendering fidelity. SEA involves introducing a compliant element between the actuator and the interaction port and utilizing the model of this compliance for closed-loop force control [1–3]. The purposeful introduction of the compliant element relaxes the stringent stability constraints on the controller gains that arise due to sensor-actuator noncollocation and actuator bandwidth restrictions [4–6] and provides high stability robustness for interaction control. Furthermore, high rendering performance can be achieved by actively compensating for the dynamics of the compliant element through the use of its model. On the negative side, the control effort required to compensate for the compliant element increases rapidly for high-frequency interactions, resulting in actuator saturation and limiting the control bandwidth of SEA.

Velocity-sourced impedance control (VSIC) is a widely used controller for SEA that utilizes a cascaded architecture. The inner motion control loop of VSIC effectively compensates for the parasitic forces, resulting in favorable rendering performance [1,3,7,8]. Additionally, VSIC does not require a dynamic model of the plant, allowing for empirically tuned controller gains.

In the literature, extensive research has been conducted on establishing passivity conditions of SEA under VSIC [9–12], and the necessary and sufficient conditions for passivity have been determined for linear spring and null impedance rendering [13,14]. It has also been proven that the passively renderable stiffness of SEA under any causal controller is limited by the physical stiffness of its compliant element [15]. Moreover, it has been shown that while Kelvin–Voigt (abbreviated as Voigt) models (linear spring and damper connected in parallel) cannot be passively rendered using SEA under VSIC with positive controller gains [11], passive Voigt model rendering that compensates for plant damping is possible with SEA under VSIC through the use of negative controller gains [14]. The passivity analysis of SEA has also been extended to model-based control, such as model reference force control [16].

Series elastic actuation relies on the assumption that its compliant element is an ideal spring and estimates the interaction forces through the deflections of this spring element for use in the closed-loop force control. However, this assumption is unrealistic, as some form of energy dissipation is inherent to all physical spring

[1]Corresponding author.
Contributed by the Dynamic Systems Division of ASME for publication in the Journal of Dynamic Systems, Measurement, and Control. Manuscript received April 22, 2024; final manuscript received April 2, 2025; published online May 16, 2025. Assoc. Editor: Neera Jain.

implementations. Furthermore, this dissipation is parallel to the series elastic element and cannot be included in the environment model during the coupled stability analysis, as commonly done for the end-effector mass. The inclusion of the physical dissipation of the elastic element in the model of the SEA has major consequences on the high-frequency response of the system model, as seen from the interaction port. One such model extends the SEA paradigm to series *damped* elastic actuation (SDEA) by incorporating a viscous dissipation element parallel to the series elastic element [17–21].

The frequency responses of SDEA and SEA are significantly different. When the causal controllers roll off, the dynamics of the uncontrolled plant are recovered; hence, the high-frequency responses of SDEA/SEA as seen from the interaction port are dominated by the dynamics of their serially attached physical filters. Accordingly, at high frequencies, the dynamics of SDEA are dominated by its damping (even for low damping coefficients), while SEA behaves as a linear spring. Consequently, SDEA possesses *distinct* stability properties and haptic rendering performance compared to SEA since the high-frequency dynamics of the plant impose fundamental limitations on the achievable control performance of any closed-loop system.

Series *damped* elastic actuation can estimate interaction forces through the sum of the forces induced on the physical spring and damper pair. Incorporating the series physical damping into the plant and its model within the closed-loop controller has been demonstrated to enhance the force control bandwidth of SEA [17]. Moreover, this approach has been shown to provide additional benefits, such as enhancing energy efficiency [19], reducing unwanted oscillations [20], mitigating the requirement for derivative control terms [21], and enabling passive Voigt model rendering with positive controller gains [14,22,23].

Passivity analysis of SDEA has been studied in the literature, but the closed-form analytic passivity conditions derived from these studies are complex and difficult to interpret [18,22–24]. Previous research has shown that Voigt models can be passively rendered using SDEA. For example, the passive range of virtual stiffness and damping parameters for SDEA under a cascaded impedance controller with an inner torque loop acting on a velocity-compensated plant and load dynamics has been presented in Ref. [24]. Similarly, a passivity analysis of SDEA under an unconventional basic impedance controller has been presented in Ref. [18]. In this controller, a force sensor is employed after the end-effector inertia to measure human interface forces and these force measurements are used in the closed-loop force control, in addition to the series-damped elastic element. The passivity analysis with this controller indicates that a sufficient level of viscous damping is required in the compliant element to ensure the passivity of stiffness rendering.

Mengilli et al. [22] have provided sufficient conditions for the passivity of SDEA under VSIC for the null impedance, linear spring, and Voigt model rendering. Furthermore, they have extended these results to absolute stability analysis and derived necessary and sufficient conditions for two-port passivity of SDEA under VSIC with a virtual coupler [23].

Recently, authors have established necessary and sufficient conditions for the passivity of SEA and SDEA (together abbreviated as S(D)EA) under VSIC while rendering Voigt, spring, and null impedance models [14]. Moreover, the use of passive physical equivalents for S(D)EA under VSIC has been advocated in Ref. [14] to establish an intuitive understanding of the passivity bounds and to highlight the effect of different plant parameters and controller terms on the closed-loop performance. Furthermore, the passive physical equivalents are shown to be instrumental in enabling objective comparisons of closed-loop systems featuring different controller architectures. In Ref. [25], authors have extended their analysis to study the effects of low-pass filtering on SEA under VSIC.

This study follows an analysis technique similar to Refs. [14,25], as it relies on frequency domain analysis to derive closed-form analytical solutions for necessary and sufficient conditions that ensure passivity, and utilizes passive physical equivalents to establish an understanding of the passivity bounds, to determine the parasitic elements, and to compare the effect of different plant and controller dynamics on the coupled stability and haptic rendering performance of the closed-loop system.

On the other hand, this study significantly extends the previously established results on the passivity analysis and passive physical realizations of S(D)EA [14,15,22,23], by establishing a fundamental rendering limitation for SDEA, proving that the inclusion of the damping of physical filter in the model enables passive rendering of Voigt models that exceed the stiffness and damping levels of the plant, and systematically studying the impact of including/omitting the damping force induced on the serial compliant element under VSIC on the rendering performance. Our novel contributions can be listed as follows:

- Utilizing a Cauchy integral, we establish a fundamental rendering limitation for all SDEA systems under causal controllers and prove that the inclusion of viscous damping of the physical filter in the model enables passive rendering of stiffness levels that are higher than the physical stiffness of the serial filter, as well as passive rendering of Voigt models whose damping levels exceed the physical damping of the plant. This relation also explains why Voigt model rendering with SEA is restricted to damping compensation.
- We present necessary and sufficient conditions for the passivity of SDEA under VSIC while rendering Voigt, spring, and null impedance models, when the damping force on the physical filter is *not* used for closed-loop control.
- We derive passive physical equivalents of various closed-loop SDEA systems and rigorously study the effect of omitting/including the damping force induced on the physical filter of SDEA in the system model on the coupled stability and closed-loop rendering performance.
- We provide comprehensive comparisons of rendering performance among various closed-loop systems with different plant models including or omitting the series damping and/or controllers utilizing different interaction force estimates through their passive physical equivalents and K-B plots.
- We demonstrate the validity and applicability of our theoretical results through a comprehensive set of experiments using a custom brake pedal with SDEA.

2 Preliminaries

A schematic representation of a single-axis plant with SDEA in the absence of its controller is presented in Fig. 1. The figure illustrates the actuator's reflected inertia J_m, viscous friction B_m which includes the motor damping, the physical spring K and the viscous damper B_f arranged in parallel between the end effector and the actuator. The actuator and end-effector velocities are represented by ω_m and ω_{end}, respectively. The symbol τ_m denotes the actuator torque, while M_{end} represents the inertia of the end effector. Consideration is given to a lumped-parameter linear time-invariant (LTI) model, so nonlinear effects, including backlash and actuator saturation, are neglected.

The torque applied to the physical filter, represented as a damped compliant element, is equal to the sum of the torques exerted on the linear spring K and the viscous damper B_f. Figure 1 can be regarded

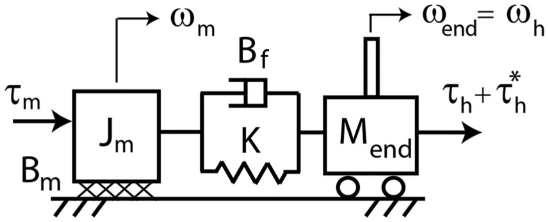

Fig. 1 Schematic representation of an SDEA plant

as a SEA when $B_f = 0$, and the torque can be estimated by the force on the spring.

Human interaction forces are divided into two components: the passive component τ_h and deliberately applied active component τ_h^*, where the former is taken to be independent of the system states, under the assumption of nonmalicious interactions. Since inanimate environments are passive and nonmalicious human interactions do not intend to destabilize a system, passivity implies coupled stability of interactions [26].

The end-effector inertia is considered as low such that $\tau_{\text{SDEA}}(s) \approx \tau_h + \tau_h^*$. Furthermore, this end-effector inertia is included in the environment for the passivity analysis as its existence does not affect the passivity conclusions. The impedance at the human interaction port is taken as $Z_{\text{out}}(s) = -\frac{\tau_{\text{sea}}(s)}{\omega_{\text{end}}(s)}$, where the interaction torque is considered as positive when in compression.

The control diagram of SDEA under VSIC, where only the elasticity of the series damped elastic element is used in the estimation of the interaction forces, denoted as $\text{SDEA}_{K_{\text{fb}}}$ under VSIC, is illustrated in Fig. 2. Here, G_t and G_m denote the torque and motion controllers, respectively. The virtual environment is assumed to have a zero motion reference ($\omega_0 = 0$). The physical plant parameters are assumed to be positive, while the controller gains are allowed to be negative, as long as the inner motion control loop is asymptotically stable. We also neglect any filtering or time delay that may be introduced during the measurement of the deflections of the physical filter and the actuator velocities. Without loss of generality, the transmission ratio of the system is set to unity.

Physical insights into the passivity-performance tradeoffs of interaction controllers can be obtained by the synthesis of passive physical equivalents, also called realizations [6,14,27].

Definition 1. *Passive physical equivalents (realizations) describe physically realizable behaviors with a network of passive fundamental elements in a domain to realize a driving-point impedance.*

The force-current analogy in the mechanical domain equates a spring to an inductor, a damper to a resistor, and mass or inertia to a *grounded* capacitor. The analogy has been extended to include an inerter element that functions like an *ungrounded* capacitor [28]. This extension is significant because it allows the use of classical electrical-domain results for synthesizing positive-real impedances with mechanical networks. Several works have leveraged inerters to design mechanical networks with desired properties [14,28–34].

Definition 2. *In the mechanical domain, an inerter is an ideal linear two-terminal energy storage element with terminal forces proportional to the relative acceleration between them.*

3 Fundamental Rendering Limitations of Series *Damped* Elastic Actuation

In the following proposition, we establish a fundamental control limitation in terms of the passive rendering bounds for Voigt and linear spring models with SDEA under any causal controller. We show that the consideration of the viscous damping effect in parallel to the compliant element fundamentally changes the bounds on the virtual environments that can be passively rendered.

Proposition 1. *Consider Voigt model rendering with an LTI SDEA plant with a casual controller such that the impedance as seen from the interaction port is $Z_{\text{SDEA}_{\text{cl}}}(s) = K_{\text{vir}}/s + B_{\text{vir}}$ up to a performance bandwidth ω_p, where K_{vir} and B_{vir} denote the constant rendered stiffness and damping levels,* respectively. *Let Ω_a denote the (finite) available bandwidth at which the high-frequency impedance at the interaction port converges to $Z_{\text{SDEA}_{\text{cl}}}(s) = K/s + B_f$, as dictated by the open loop dynamics of SDEA with a physical filter consisting of K and B_f pair in parallel. Then, the following inequality establishes a fundamental bound for the passive rendering with SDEA:*

$$\frac{\pi}{2} K + \Omega_a B_f \geq \frac{\pi}{2} K_{\text{vir}} + \omega_p B_{\text{vir}}$$

The proof of Proposition 1 is presented in the Appendix A.

Proposition 1 establishes that, unlike the case for SEA, where $B_f = 0$, there exist causal controllers for which it is possible to passively render virtual stiffness levels K_{vir} that are higher than the physical stiffness K of the series elastic element; hence, the addition of B_f can significantly relax the passivity bound on spring rendering with SEA [15].

Furthermore, given that, in general, the available bandwidth Ω_a is much higher than the performance bandwidth ω_p, Proposition 1 further indicates that damping levels exceeding B_f are possible, even for high K_{vir}. Accordingly, while SEA can only compensate for the plant damping [14], SDEA can also augment it.

Finally, Proposition 1 enforces that the upper bound on K_{vir} decreases as B_{vir} increases during Voigt model rendering.

4 Passivity and Physical Equivalents of $\text{SDEA}_{K_{\text{fb}}}$

In this section, we study the effect of omitting the damping force induced on the series damped compliant element in closed-loop control and provide necessary and sufficient conditions for the passivity. The model in Fig. 2, named $\text{SDEA}_{K_{\text{fb}}}$ under VSIC, captures the most common implementation of SEA, where the inherent damping effect on the serial elastic element is ignored during the controller implementation.

The impedance at the interaction port of $\text{SDEA}_{K_{\text{fb}}}$ under VSIC during Voigt model rendering when both controllers are proportional is

$$Z_{\text{Voigt}}^{\text{SDEA}_{K_{\text{fb}}}}(s) = \frac{B_f J_m s^3 + \big(B_f(B_m + G_m + B_{\text{ref}}\,\alpha) + J_m K\big) s^2 + \big(K(B_m + G_m) + \alpha(B_{\text{ref}} K + B_f K_{\text{ref}})\big) s + K K_{\text{ref}}\,\alpha}{J_m s^3 + (B_f + B_m + G_m) s^2 + K(1+\alpha) s} \quad (1)$$

where $\alpha = G_m G_t$.

4.1 Passivity of $\text{SDEA}_{K_{fb}}$ During Voigt Model Rendering.

Proposition 2 presents necessary and sufficient conditions for the passivity of $\text{SDEA}_{K_{fb}}$ under VSIC while rendering Voigt models. The inner motion control loop is considered to be asymptotically stable by imposing $(B_m + G_m) > 0$.

Proposition 2. *Consider Voigt model rendering for $\text{SDEA}_{K_{fb}}$ under VSIC as in Fig. 2, where G_t and G_m consist of proportional gains. Let the physical plant parameters be positive, while the controller gains are allowed to be negative as long as the inner*

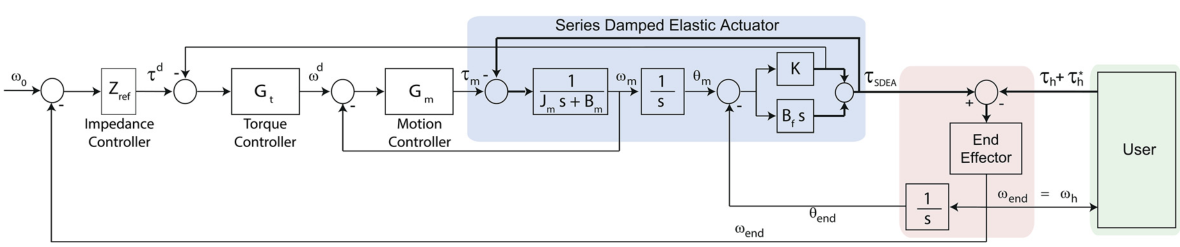

Fig. 2 Block diagram of $\text{SDEA}_{K_{\text{fb}}}$ under VSIC, for which the interaction forces are estimated by only utilizing the deflections of the physical spring and omitting the damping of the physical filter

Table 1 Comparison of physical realizations of various models of S(D)EA under VSIC

<table>
<tr><th></th><th>Voigt rendering</th><th>Spring rendering</th><th>Null rendering</th></tr>
<tr><td>SEA[a]</td><td>(a)
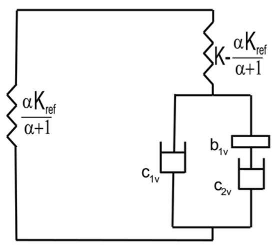</td><td>(b)
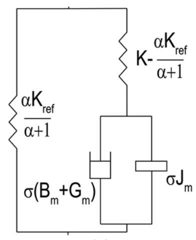</td><td>(c)
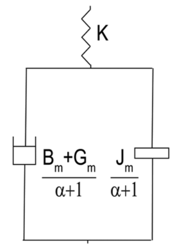</td></tr>
<tr><td>SDEA[a]</td><td>(d)
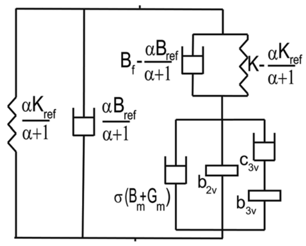</td><td>(e)
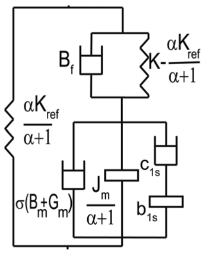</td><td>(f)
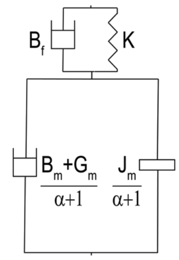</td></tr>
<tr><td>SDEA$_{K_{fb}}$</td><td>(g)
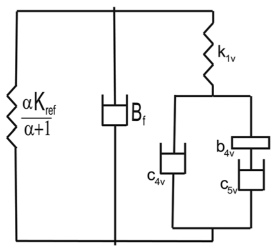</td><td>(h)
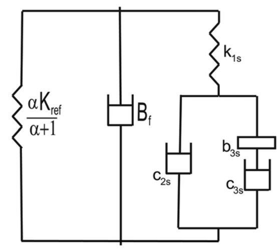</td><td>(i)
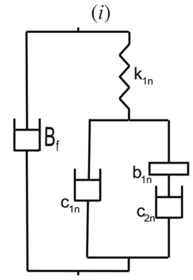</td></tr>
</table>

[a]The realizations of S(D)EA under VSIC presented in (*a*)–(*f*) tabs are adapted from [14].

motion control loop is asymptotically stable. Then, the following inequalities serve as necessary and sufficient conditions for establishing the passivity of $Z^{\mathrm{SDEA}_{K_{fb}}}_{\mathrm{Voigt}}(s)$.

(i) $K \geq K_{\rm ref}\,\frac{\alpha}{(\alpha+1)}\,\frac{B_m+G_m-B_f\,\alpha}{B_m+G_m+B_{\rm ref}\,\alpha}$, *and*

(ii) $-(B_m+G_m) < \alpha\,B_{\rm ref}$, *and*

(iii) $0 < \frac{\alpha}{\alpha+1}K_{\rm ref}$, *and*

(iv) $0 < (\alpha+1)$, *and*

(v) $0 < (B_m+G_m)$, *and*

(vi) $-2\sqrt{\gamma} \leq B_f\,(B_m+G_m+B_{\rm ref}\alpha)\,(B_f+B_m+G_m) - \alpha\,J_m\,(B_f(K+K_{\rm ref})+KB_{\rm ref})$

where $\gamma = B_f J_m{}^2\left(K(\alpha+1)(K(B_m+G_m+B_{\rm ref}\alpha)+B_f\alpha K_{\rm ref}\right) - \alpha K K_{\rm ref}\,(B_f+B_m+G_m)$.

The proof of Proposition 2 is presented in Appendix B.

Remark 1 (1). If $B_{\rm ref}$ ($B_{\rm ref}$ and $K_{\rm ref}$) is set to zero in Eq. (1), the output impedance transfer function becomes the same as the transfer function for spring (null impedance) rendering. Hence, Proposition 2 covers spring and null impedance rendering as its special cases.

Together with Condition (i), a simpler but more conservative set of sufficient conditions can be derived by imposing the following inequality instead of Condition (ii) of Proposition 2:

$$J_m \leq \frac{B_f\,(B_f+B_m+G_m)\,(B_m+G_m+B_{\rm ref}\,\alpha)}{\alpha\,(K\,(B_{\rm ref}+B_f)+B_f\,K_{\rm ref})} \tag{2}$$

4.2 Passive Physical Equivalent of SDEA$_{K_{fb}}$ Under Velocity-Sourced Impedance Control.

A realization of Eq. (1) characterizing SDEA$_{K_{fb}}$ under VSIC during Voigt model rendering is presented in Table 1(*g*). The parameters of this realization include $k_{1v} = K - \frac{K_{\rm ref}\,\alpha}{\alpha+1} - \frac{B_f\,(B_f-B_{\rm ref}\,\alpha)}{J_m}$ and $c_{4v} = \frac{B_m-B_f+G_m+B_{\rm ref}\,\alpha-B_f\,\alpha}{\alpha+1} - \frac{K_{\rm ref}\,\alpha\,(B_m+G_m-B_f\,\alpha)}{K\,(\alpha+1)^2}$. The rest of the terms are relatively complicated; hence, they are presented as a MATLAB script that allows for a numerical means of checking for the non-negativeness of each element[2].

The third row of Table 1 presents realizations of SDEA$_{K_{fb}}$ under VSIC while rendering Voigt, spring, and null impedance models. Table 1 indicates that there exists continuity among the realizations; the realization of spring rendering and null impedance rendering with SDEA$_{K_{fb}}$ can be recovered from Voigt model rendering with SDEA$_{K_{fb}}$ by setting $B_{\rm ref} = 0$ and $B_{\rm ref} = K_{\rm ref} = 0$, respectively. Realizations of SEA can also be recovered from the realizations of SDEA$_{K_{fb}}$ by setting $B_f = 0$.

4.3 Effective Impedance Analysis.

After removing the rendered stiffness and physical damper pair $\frac{\alpha}{(\alpha+1)}\,K_{\rm ref}$–$B_f$ and the serial coupling filter k_{1v}, the effective impedance of the realization in Table 1(*g*) indicates that the effective damping converges to c_{4v} at low frequencies, while it approaches to $c_{4v}+c_{5v}$ at high frequencies. Accordingly, for these elements, c_{4v} is the dominant damping at low

[2]The MATLAB script of the parameters of the realization in Table 1*g* is available for download at https://hmi.sabanciuniv.edu/SDEAKfb_realization.m.

frequencies, and c_{5v} is added to c_{4v} as the frequency increases. Similarly, the effective parasitic inertance converges to b_{4v} at low frequencies, while it approaches zero at high frequencies. While the effect of b_{4v} becomes higher as the frequency increases, this is balanced by the fact that effective inertance goes to zero at high frequencies.

4.4 Haptic Rendering Performance. The physical realization of SDEA$_{K_{fb}}$ during Voigt model rendering in Table 1(*g*) indicates three main branches in parallel: a spring-damper pair $\frac{\alpha}{(\alpha+1)} K_{\text{ref}}$–$B_f$ in parallel, and a branch capturing the dynamics governed by a complex topology of damper-inertance terms that are coupled to the system in series through a spring. The effective impedances at low and high frequencies of the complex topology of damper-inertance terms are provided in the Sec. 4.3.

The parallel spring-damper pair of $\frac{\alpha}{(\alpha+1)} K_{\text{ref}}$–$B_f$ indicates that SDEA$_{K_{fb}}$ under VSIC can render the desired spring levels for proper selections of K_{ref}. Rendering of desired damping levels is more involved as both c_{4v} and c_{5v} depend on B_{ref}. At low frequencies, the effective impedance of the whole system approaches $B_f + c_{4v}$ (B_{vir}); hence, B_{ref} can be selected to render desired damping levels. Even though the presented realization is only valid for positive values of c_{4v}, passivity conditions indicate that it is possible to render desired damping levels that are lower than the damping of the series elastic element by selecting c_{4v} negative, such that $0 > c_{4v} \geq -B_f$.

Note that the inerter-damping terms are coupled to $\frac{\alpha}{(\alpha+1)} K_{\text{ref}}$–$B_f$ in parallel through the coupling filter k_{1v} and this coupling becomes stronger for lower choices of K_{ref}. As frequency increases, c_{5v} is added to rendered damping as a parasitic effect. Unlike the case in SDEA realization, SDEA$_{K_{fb}}$ realization does not have a pure inerter term that dominates the parasitic dynamics at high frequencies; similar to SEA realization, SDEA$_{K_{fb}}$ realization has an inerter term b_{4v} that adds frequency dependent inertance at low frequencies.

A comparison of the effective impedances of the realization of SDEA$_{K_{fb}}$ with SDEA under VSIC indicates that while the effective parasitic inertance of SDEA$_{K_{fb}}$ goes to zero, the effective parasitic inertance of SDEA goes to b_{2v} at high frequencies; hence, the parasitic inertance of SDEA is higher than that of SDEA$_{K_{fb}}$. A numerical comparison of the effective parasitic damping of SDEA$_{K_{fb}}$ with SDEA under VSIC is presented in Sec. 5.

4.5 Comparison of Passivity Bounds of SDEA$_{K_{fb}}$ With Series *Damped* Elastic Actuation. For the simplicity of the analysis, a comparison is made for the case when all controller gains are taken positive. Comparison of the necessary conditions presented for SDEA in Ref. [14] and Condition (i) of Proposition 2 that impose upper bounds on K_{ref} for SDEA$_{K_{fb}}$ indicates that the bound for SDEA$_{K_{fb}}$ is more relaxed as follows:

$$K \geq K_{\text{ref}} \frac{\alpha}{(\alpha+1)} \frac{B_m + G_m}{B_m + G_m + B_{\text{ref}}\,\alpha} \geq K_{\text{ref}} \frac{\alpha}{(\alpha+1)} \frac{B_m + G_m - B_f \alpha}{B_m + G_m + B_{\text{ref}}\,\alpha} \tag{3}$$

Accordingly, Eq. (3) shows that SDEA$_{K_{fb}}$ can passively render virtual springs that are stiffer than the virtual springs that can be passively rendered by SDEA. In fact, with SDEA$_{K_{fb}}$ under VSIC, it is possible to passively render virtual stiffness levels that exceed the stiffness of the physical filter.

Comparison of the sufficient conditions of SDEA and SDEA$_{K_{fb}}$ presented in Ref. [14] and Eq. (2) indicate that

$$J_m \leq \frac{B_f\,(B_m + G_m + B_{\text{ref}}\,\alpha)\,\left[B_m + G_m + B_f\,(1+\alpha)\right]}{(B_f\,K_{\text{ref}} + B_{\text{ref}}\,K)\,\alpha} \leq \frac{B_f\,(B_m + G_m + B_{\text{ref}}\,\alpha)\,(B_m + G_m + B_f)}{\left[B_f\,K_{\text{ref}} + K\,(B_{\text{ref}} + B_f)\right]\alpha} \tag{4}$$

Table 2 Plant parameters utilized in simulations

Parameter (unit)	Value	Parameter (unit)	Value
J_m (kgm^2)	0.002	B_m (Nms/rad)	1.22
K (Nm/rad)	360	B_f (Nms/rad)	0.35

Consequently, while SDEA$_{K_{fb}}$ can passively render a larger range of virtual springs compared to SDEA according to Eq. (3), SDEA$_{K_{fb}}$ also possesses a more strict passivity bound on J_m as expressed in Eq. (4).

5 Evaluations of Rendering Performance

This section studies the haptic rendering performance by providing comparisons of Bode plots of the S(D)EA models under VSIC during Voigt model, linear spring, and null impedance rendering.

Table 2 presents the plant parameters utilized in the simulations. The controller gains of VSIC are taken as $G_m = 10$ Nms/rad and $G_t = 5$ rad/(sNm). The Voigt model parameters are chosen as $K_{\text{ref}} = 150$ Nm/rad and $B_{\text{ref}} = 0.1$ Nms/rad, respectively. For SEA, B_{ref} is set to -0.0307 Nms/rad such that $c_{1v} = 0.1$ Nms/rad.

Performance evaluations of rendering with S(D)EA under VSIC, with the insights provided by their passive physical equivalents, have been presented in Ref. [14].

5.1 Effect Physical Filter Damping on Series *Damped* Elastic Actuation and SDEA$_{K_{fb}}$. Tables 1(*d*)–1(*f*) present the passive physical equivalents of SDEA under VSIC during Voigt model, spring, and null impedance rendering, respectively. Figure 3 exhibits the performance of Voigt model, spring, and null impedance rendering for SDEA, while employing proportional controllers. Results in Fig. 3(*a*) indicate that the Voigt model rendering performs poorly for the lowest value of B_f, but there is no noticeable distinction between rendering performance for sufficiently high B_f, such as when $B_f = 0.5$ Nms/rad and 1 Nms/rad. Moreover, Fig. 3(*b*) reveals that when B_f is minimum, the performance bandwidth of spring rendering is the largest, but the fidelity of spring rendering diminishes for larger virtual springs. Similarly, Fig. 3(*c*) shows that the null impedance rendering performs poorly for the lowest B_f, but there is no significant difference between the rendering performance when $B_f = 0.5$ Nms/rad and 1 Nms/rad.

Tables 1(*g*)–1(*i*) present the passive physical equivalents of SDEA$_{K_{fb}}$ under VSIC during Voigt model, spring, and null impedance rendering, respectively. All passive physical equivalents have the damping of the physical filter B_f as a term parallel to all other terms. Passive physical equivalents make it explicit that B_f is directly included in the effective damping of SDEA$_{K_{fb}}$.

Figure 4 illustrates the effects of varying B_f on the performance of Voigt model, spring, and null impedance rendering for SDEA$_{K_{fb}}$. Figures 4(*a*) and 4(*b*) indicate that decreasing B_f results in a larger performance bandwidth for virtual spring rendering. Similarly, Fig. 4(*c*) demonstrates that decreasing B_f leads to improvements in the null impedance rendering.

Figures 3 and 4 illustrate that the rendering performance of SDEA increases for higher B_f, while the performance of SDEA$_{K_{fb}}$ decreases for higher B_f. This observation can be explained by examining the realizations of both systems. Specifically, B_f acts as an uncontrolled term that runs parallel to controlled damping of c_{4v} for SDEA$_{K_{fb}}$ and higher B_f values require larger adjustments to c_{4v} to overcome effects of B_f. Conversely, for SDEA, there is a direct control action on the B_f that can be used to improve the rendering performance.

Figures 3 and 4 also demonstrate that SEA approaches its physical stiffness K at high frequencies, while the presence of even a low B_f changes the high-frequency behavior, with both SDEA and SDEA$_{K_{fb}}$ converging to B_f.

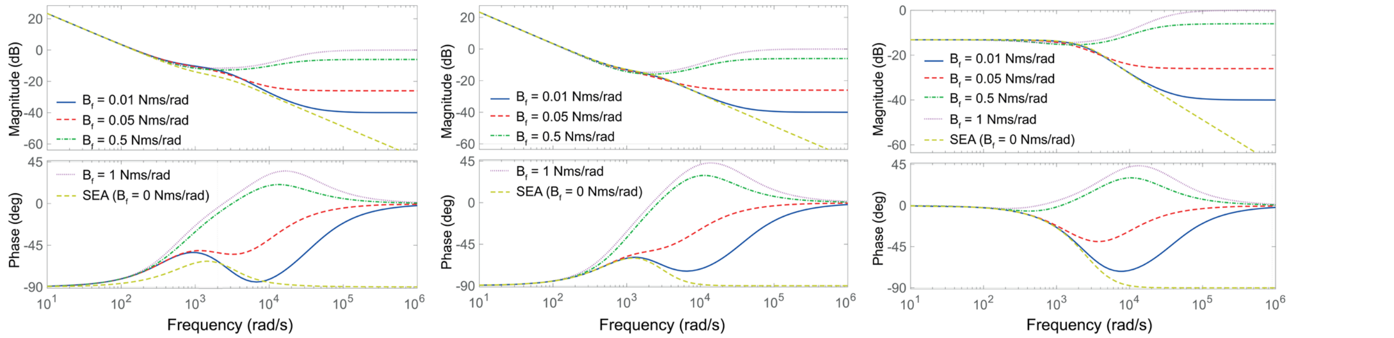

(*a*) (*b*) (*c*)

Fig. 3 Effect of physical filter damping B_f on performance SDEA during Voigt, spring, and null impedance rendering: (*a*) Voigt model rendering, (*b*) spring rendering, and (*c*) null impedance rendering

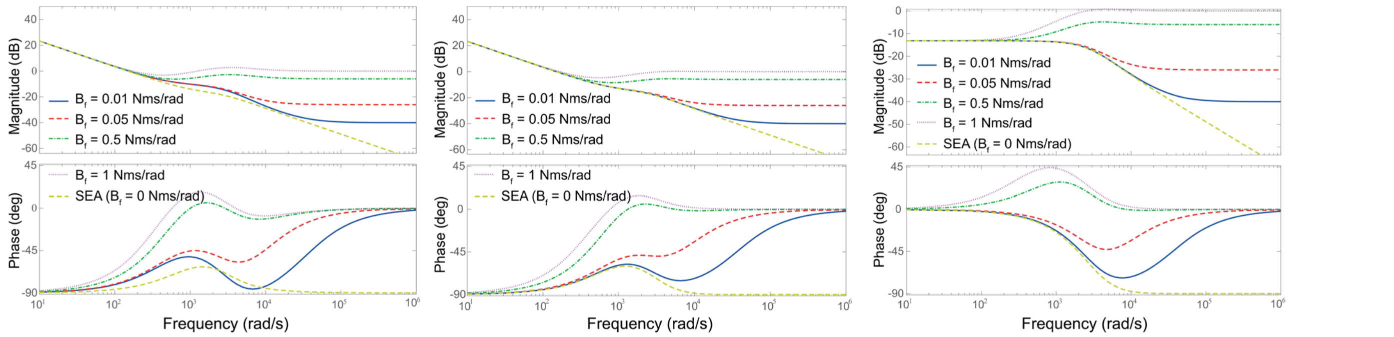

(*a*) (*b*) (*c*)

Fig. 4 Effect of unmeasured B_f on the performance of SDEA$_{K_{fb}}$ during Voigt, spring, and null impedance rendering: (*a*) Voigt model rendering, (*b*) spring rendering, and (*c*) null impedance rendering

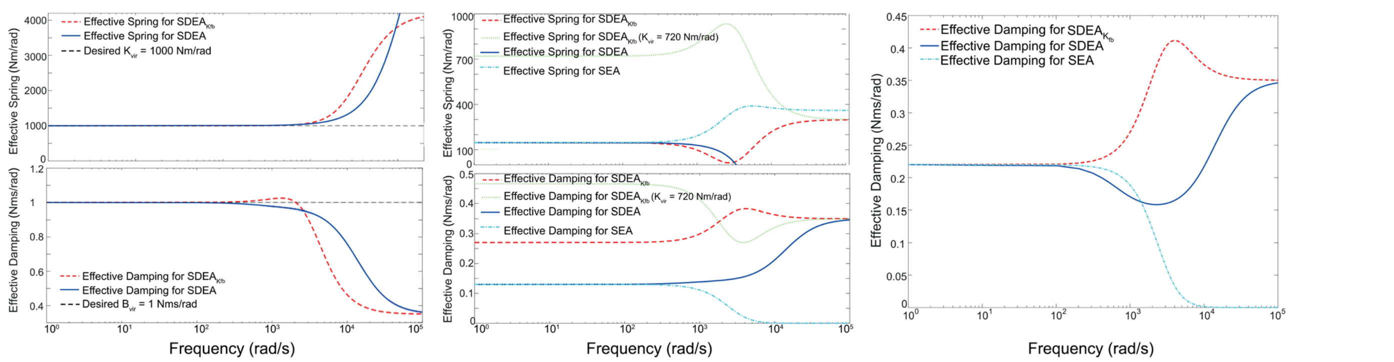

(*a*) (*b*) (*c*)

Fig. 5 Effective impedance comparisons of the S(D)EA models under VSIC: (*a*) effective impedances for SDEA and SDEA$_{K_{fb}}$ during Voigt model rendering, (*b*) effective impedances for S(D)EA and SDEA$_{K_{fb}}$ during spring rendering, and (*c*) effective damping of S(D) EA and SDEA$_{K_{fb}}$ during null impedance

5.2 Comparisons of Series *Damped* Elastic Actuation, SDEA$_{K_{fb}}$, and Series Elastic Actuation

5.2.1 Voigt Model Rendering. The passive realizations of the S(D)EA models during Voigt model rendering are presented in Tables 1(*a*), 1(*d*), and 1(*g*), respectively.

Table 1(*d*) presents a realization featuring a controllable damping term alongside a controllable stiffness term, allowing for direct rendering of desired virtual springs and dampers. In contrast, Table 1(*g*) exhibits realizations with controllable stiffness terms for rendering desired virtual springs, but the damping terms include the parasitic damping B_f of the physical filter in parallel with the controllable damping terms. Although this configuration still facilitates the rendering of desired damping levels for SDEA$_{K_{fb}}$, the control is more indirect and require suppression of B_f.

Figure 5(*a*) depicts comparisons of the Voigt model rendering performance of SDEA and SDEA$_{K_{fb}}$ in terms of their effective impedances. SEA is not presented in Fig. 5(*a*) because damping augmentation is not possible for SEA. Desired damping and stiffness values are set to 1 Nms/rad and 1000 Nm/rad for Fig. 5(*a*), respectively. The appropriate B_{ref} are selected such that $B_f + c_{4v} = B_{\text{vir}} = 1$ Nms/rad for SDEA$_{K_{fb}}$ and $\frac{\alpha}{\alpha+1}B_{\text{ref}} + \sigma(B_m + G_m) = B_{\text{vir}} = 1$ Nms/rad for SDEA. The desired damping value is almost 5 times the parasitic damping value in Table 1(*f*) and the desired stiffness value

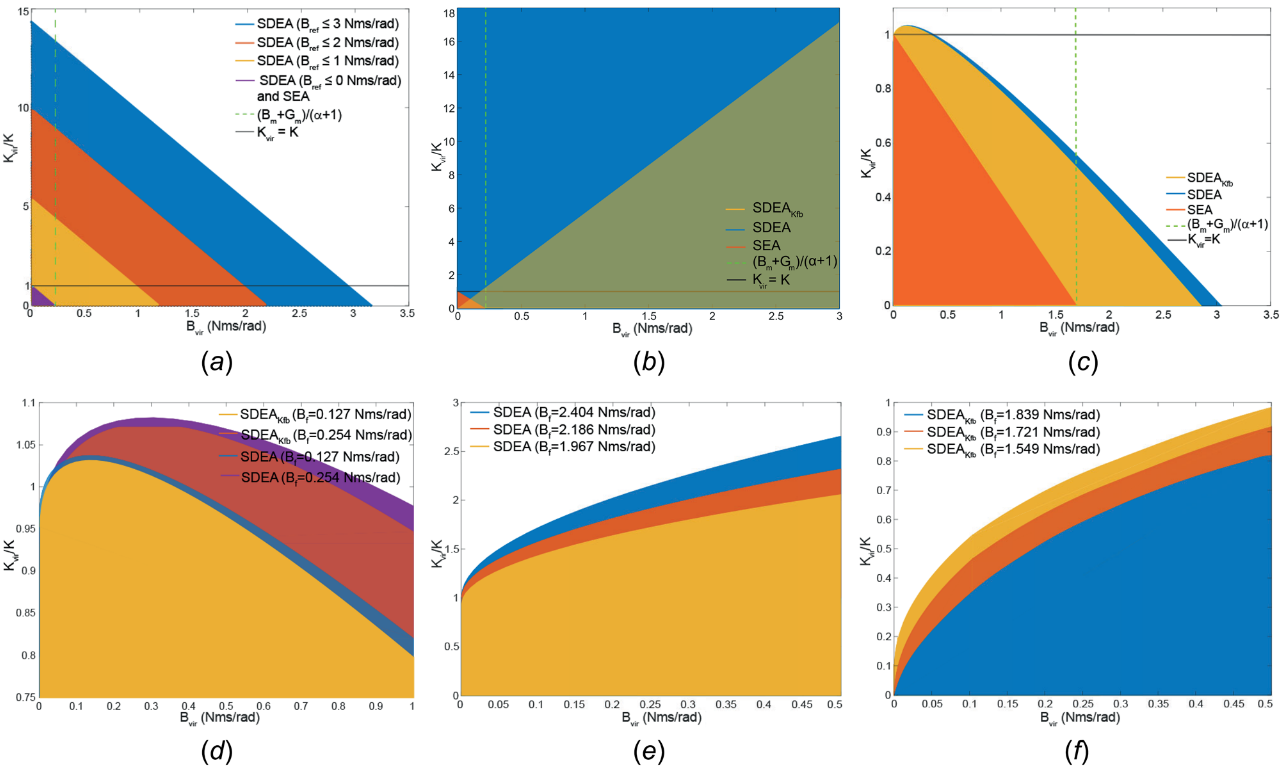

Fig. 6 K-B plots of the S(D)EA models under VSIC: (*a*) K-B plots for S(D)EA under VSIC for var. B_{ref}, (*b*) K-B plots for S(D)EA & SDEA$_{K_{fb}}$ for high B_f, (*c*) K-B plots for SDEA & SDEA$_{K_{fb}}$ for low B_f, (*d*) K-B plots for SDEA & SDEA$_{K_{fb}}$ for various B_f, (*e*) K-B plots of SDEA around the critical B_f, and (*f*) K-B plots of SDEA$_{K_{fb}}$ around the critical B_f

is almost three times the physical stiffness of the plant. The results indicate that SDEA$_{K_{fb}}$ has a similar performance bandwidth to SDEA in terms of achieving the desired damping level and virtual stiffness, but SDEA has slightly better accuracy, as shown in Fig. 5(*a*).

Figure 6(*a*) presents K-B plots for S(D)EA for various B_{ref} values. The lowest B_{ref} value for the K-B plots of SEA and SDEA is set to $-\frac{B_m+G_m}{\alpha}$ according to the passivity condition. The area under the K-B plot of SDEA increases as B_{ref} increases, as shown in Fig. 6(*a*). During physical implementations, the unmodeled actuator saturation will introduce an upper bound to this K-B plot. The K-B plot of SEA is a subset of that of SDEA since only *damping compensation* is possible with SEA, while *damping augmentation* is also possible with SDEA. In particular, SEA can passively render virtual damping levels from zero to $\frac{B_m+G_m}{\alpha+1}$, while its virtual stiffness needs to simultaneously decrease from its highest value of K to zero, that is, the highest virtual damping rendering requires zero stiffness, while the highest stiffness rendering necessitates zero virtual damping.

Figure 6(*b*) depicts K-B plots of the S(D)EA models for relatively high values of B_f. In this figure, the K-B plot of SDEA covers the whole plot, as no actuator saturation is imposed, while the K-B plot of SEA only covers the damping compensation region as in Fig. 6(*a*). The K-B plot of SDEA$_{K_{fb}}$ is depicted by the yellow triangle, which indicates that SDEA$_{K_{fb}}$ can passively render high virtual stiffness levels with high virtual damping, but unlike the case for SDEA, SDEA$_{K_{fb}}$ cannot passively render high K_{vir} with low B_{vir}.

Figures 6(*c*)–6(*f*) depict K-B plots of the S(D)EA models using the physical filter damping $B_f = 0.127$ Nms/rad of the experimental setup and gains presented in Sec. 6. Unlike the case in K-B plots presented in Fig. 6(*b*), higher K_{vir} is limited by B_{vir} for SDEA and SDEA$_{K_{fb}}$, as presented in Fig. 6(*c*). SDEA$_{K_{fb}}$ and SDEA have similar performance for the lower B_{vir}, but SDEA can reach a higher B_{vir} than SDEA$_{K_{fb}}$ for the same K_{vir} levels. B_{vir} and K_{vir} ranges for SEA are constrained by $\frac{B_m+G_m}{\alpha+1}$ and physical stiffness K, respectively, as in Fig. 6(*b*).

Figure 6(*d*) illustrates K-B plots for SDEA and SDEA$_{K_{fb}}$ for various levels of B_f. It demonstrates that as B_f decreases, the K_{vir}/K ratio approaches unity, while the peak stiffness level decreases. Moreover, the total area increases for higher B_f, for both SDEA and SDEA$_{K_{fb}}$, with the peak stiffness of SDEA surpassing that of SDEA$_{K_{fb}}$. Figures 6(*a*)–6(*d*), indicate that B_f directly influences the shape of K-B plots.

Figure 6(*e*) presents K-B plots of SDEA, as B_f approaches the critical point where the change in passivity bounds occurs. In particular, when B_f exceeds a critical value, Condition (i) of Proposition 1 in Ref. [14] becomes more conservative than Condition (v) of Proposition 1. Beyond this B_f value, the K-B plots in Figs. 6(*c*) and 6(*e*) begin to resemble the K-B plots in Fig. 6(*b*). Similarly, Fig. 6(*f*) depicts the scenario where B_f approaches its critical for SDEA$_{K_{fb}}$. This limit is determined as $\frac{B_m+G_m}{\alpha}$, which alleviates the need to impose Condition (i) of Proposition 2. Beyond this critical value, the K-B plots in Figs. 6(*c*) and 6(*f*) begin to resemble the K-B plots Fig. 6(*b*).

As B_f approaches zero, the K-B plots of SDEA and SDEA$_{K_{fb}}$ converge to the K-B plot of SEA.

5.2.2 *Spring Rendering*. Tables 1(*b*), 1(*e*), and 1(*h*) present the passive physical equivalents for spring rendering with the S(D)EA models. All passive physical equivalents have a controllable stiffness term, in parallel to all other terms. The realization in Table 1(*h*) has the filter damping B_f as parallel parasitic dynamics to the controllable stiffness, negatively affecting the rendering performance.

Figure 5(*b*) depicts the spring rendering performances of the S(D) EA models in terms of effective impedances. While the effective damping of SDEA and SEA is similar, SDEA$_{K_{fb}}$ exhibits higher effective damping, indicating higher parasitic damping effects. Figure 5(*b*) demonstrates that at low frequencies, effective damping equals $c_{2s} + B_f$. Moreover, Fig. 5(*b*) illustrates that SDEA and SEA can render the desired virtual stiffness over a wider frequency range compared to SDEA$_{K_{fb}}$. Specifically, SDEA$_{K_{fb}}$ renders a virtual stiffness level that is twice as high as the physical stiffness, depicted in Fig. 5(*b*). At high frequencies, the effective stiffness of SDEA

Table 3 Parameters of the brake pedal with SDEA

Parameter (unit)	Value	Parameter (unit)	Value
J_m (kgm^2)	0.0024	B_m (Nms/rad)	0.0177
K (Nm/rad)	121.8	B_f (Nms/rad)	0.0127

converges to zero, SDEA$_{K_{fb}}$ converges to a nonzero value, and SEA converges to its physical stiffness K, while effective damping of SDEA and SDEA$_{K_{fb}}$ converges to B_f and SEA converges to zero.

5.2.3 Null Impedance Rendering. Tables 1(*c*), 1(*f*), and 1(*i*) present the realizations for null impedance rendering for the S(D)EA models. In the realization of SDEA and SDEA$_{K_{fb}}$, B_f term is uncontrollable, but it is serially connected to the parasitic device dynamics, similar to the physical stiffness, for SDEA, while B_f is parallel to other terms for SDEA$_{K_{fb}}$. Figure 5(*c*) depicts the comparison of the S(D)EA models during null impedance rendering in terms of effective damping of the models. Effective damping of all three models approach $\frac{B_m+G_m}{\alpha+1}$ (which is also equal to $c_{1n}+B_f$) at low frequency range, but the effective damping levels of SDEA and SEA get lower at the intermediate frequency range, while the effective damping of SDEA$_{K_{fb}}$ increases. At high frequencies, effective damping converges to B_f for SDEA and SDEA$_{K_{fb}}$, while SEA converges to zero.

6 Experimental Validations

This section presents experimental validations of the theoretical passivity bounds and haptic rendering performance. The experimental setup comprises a custom single-axis brake pedal with SDEA, based on prior designs [35,36]. The pedal is actuated by a brushless DC motor equipped with an optical encoder and Hall-effect sensors. The torque output of the motor is amplified by a transmission ratio of 1:39.5. The spring of the series elastic element is implemented as a compliant cross-flexure joint, whose deflections are measured by an encoder to estimate the interaction torques. An eddy-current damper is implemented using permanent magnets and an aluminum plate. The parameters of the SDEA plant are experimentally determined as in Table 3 [14].

Velocity-sourced impedance control controllers are implemented using a real-time operating system with a sampling rate of 1 kHz using an industrial PC connected to an EtherCAT bus. Unless specified otherwise, the controller gains of VSIC are taken as $G_m = 0.0576$ Nms/rad and $G_t = 30$ rad/(sNm) throughout the experiments.

The transmission ratio of the plant was set to unity while deriving the theoretical passivity bounds. The results can be extended to systems with a transmission ratio of n by applying the following transformations to form an equivalent system: $J_{m_{eq}} = n^2 J_m$, $B_{m_{eq}} = n^2 B_m$, $G_{m_{eq}} = n^2 G_m$, and $G_{t_{eq}} = 1/n\, G_t$.

6.1 Verification of Theoretical Passivity Bounds of SDEA$_{K_{fb}}$. The passivity of a system is investigated by studying the coupled stability of interactions when the system is exposed to the most destabilizing environments [37]. This approach allows for the conclusion of system's passivity if there exists no set of ideal springs or inertias that destabilizes the system. For S(D)EA, the most destabilizing environments are inertial [13,14,23,38].

To verify the passivity bounds in Sec. 4, the SDEA brake pedal underwent testing with various inertial environments. The coupled stability conclusions for each data point in these plots were made after a search in the parameter space. Four distinct masses were coupled to the end effector of the SDEA brake pedal, and impacts were imposed on the end effector to excite the system at all possible frequencies. A line search was conducted along the y-axis, starting from 25% below the most conservative theoretical passivity bound and K_{vir} was increased with a resolution of 0.5 Nm/rad. For each trial parameter set, if no violation of the coupled stability was observed after five trials at each end-effector inertia, then it was concluded that the experimental evidence indicates passivity. Otherwise, if any violation of coupled stability was observed, then the parameter set is active. Supplementary materials including videos of experiments are available at our website[3].

6.1.1 Voigt Model Rendering. In these experiments, we have investigated the coupled stability of SDEA$_{K_{fb}}$ under VSIC during Voigt model rendering when the controllers are proportional. To validate the necessary and sufficient conditions provided in Proposition 2, we have tested various K_{ref} and B_{ref} values.

Figure 7(*a*) illustrates the experimental K_{vir}–B_{ref} plot for the brake pedal with SDEA$_{K_{fb}}$ under VSIC. The theoretical passivity bound based on Condition (i) of Proposition 2 is represented by the magenta line, while the bound based on Condition (ii) of Proposition 2 is depicted by the blue line. The experimental results confirm the theoretically predicted passivity boundary. Specifically, the experimental data conform to the dashed blue line, which is the more conservative necessary condition. The experimental results closely align with the theoretical values, with an error of about 8%. The experimental results are expected to be more conservative due to unmodeled Coulomb friction and hysteresis effects that result in additional dissipation in the physical system that cannot be accommodated in the LTI plant model.

Figure 7(*b*) presents the experimentally determined K-B plot of SDEA$_{K_{fb}}$ under VSIC, where B_{vir} is computed from $c_{4v}+B_f$ according to Table 1(*g*). Figure 7(*b*) shows that B_{vir} can be compensated with SDEA$_{K_{fb}}$ by choosing the appropriate B_{ref}. It can also be verified that K_{vir} can exceed the physical stiffness for lower B_{vir} levels, and K_{vir} decreases as B_{vir} increases.

6.1.2 Spring Rendering. In these experiments, the coupled stability of SDEA$_{K_{fb}}$ under VSIC during spring rendering when the controllers are proportional has been studied. We have selected various K_{ref} values for several G_t gains according to the conditions given in Proposition 2 when $B_{ref}=0$.

Figure 7(*c*) presents the experimental K_{vir}–G_t plot for the SDEA$_{K_{fb}}$ brake pedal under VSIC. The theoretical passivity bounds derived from Conditions (i)–(ii) of Proposition 2 when $B_{ref}=0$ are depicted as the magenta and blue lines, respectively. It can be observed that the two bounds are very close to each other for the given the parameters of the brake pedal. The experimental results validate the theoretically predicted passivity boundary; the theoretical bounds are approximately 6.5% more conservative than the experimental results.

Figure 7(*c*) also illustrates the experimentally determined bounds for coupled stability of the S(D)EA models under VSIC. As expected from the theoretical analysis, the passivity bounds for virtual spring stiffness are the highest for SDEA$_{K_{fb}}$.

6.1.3 Null Impedance Rendering. In these experiments, the coupled stability of SDEA$_{K_{fb}}$ under VSIC during null impedance rendering when the controllers are proportional has been studied. According to the theoretical bounds, SDEA$_{K_{fb}}$ during null impedance rendering is passive for all G_t values as established in Proposition 2 with $B_{ref}=K_{ref}=0$. Our experiments validate this prediction by displaying coupled stability for all the G_t gains tested.

6.2 Evaluation of Haptic Rendering Fidelity. In this subsection, we experimentally evaluate the performance of SDEA$_{K_{fb}}$ under VSIC during null impedance, spring, and Voigt model rendering. We also compare the haptic rendering performance of SDEA$_{K_{fb}}$ with SDEA under VSIC.

6.2.1 Null Impedance Rendering Performance. The null impedance rendering is valuable as it allows the user to move the end-effector with minimal resistance. An experimental validation of the null impedance rendering performance of SDEA$_{K_{fb}}$ under VSIC is demonstrated in Fig. 8(*a*), utilizing three different levels of the

[3]https://hmi.sabanciuniv.edu/SDEAKfb_EffectofDamping_Supplementary.mp4

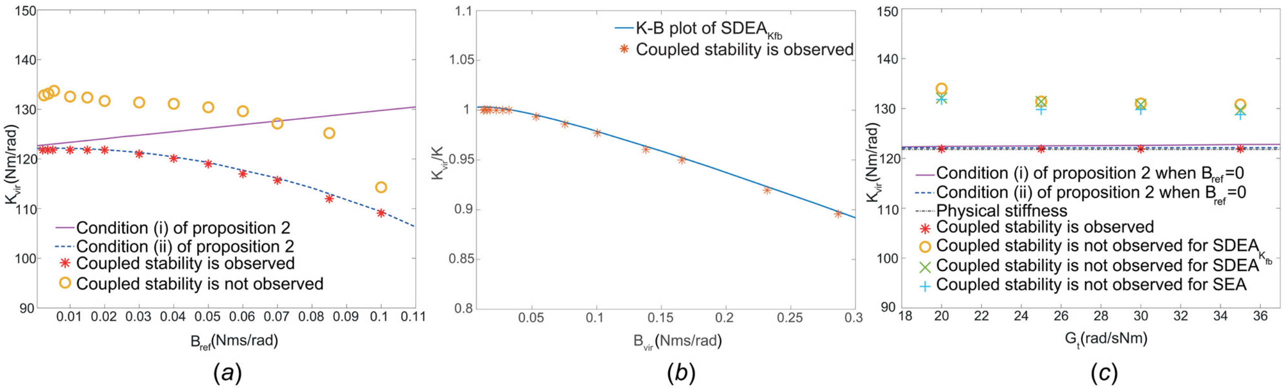

Fig. 7 Passivity bounds versus experimental coupled stability results: (*a*) B_{ref}–K_{vir} plot for SDEA$_{K_{fb}}$ during Voigt model rendering, (*b*) K-B plot of SDEA$_{K_{fb}}$, and (*c*) G_t–K_{vir} plot for SDEA$_{K_{fb}}$ during spring rendering

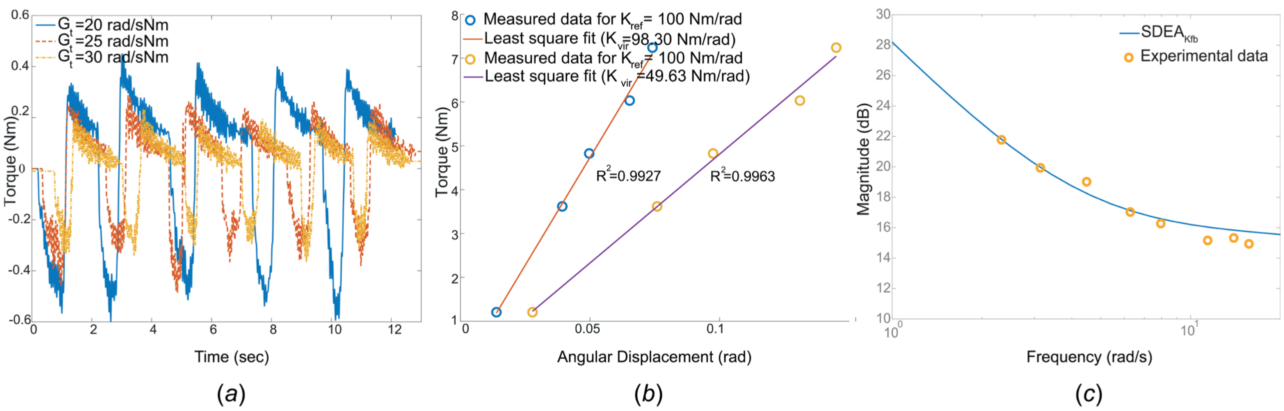

Fig. 8 (*a*) Null impedance rendering performance of SDEA$_{K_{fb}}$ for G_t = 20, 25, and 30 rad/(sNm), (*b*) virtual stiffness rendering performance of SDEA$_{K_{fb}}$ for K_{ref} = 50 and 100 Nm/rad, and (*c*) Voigt model rendering performance of SDEA$_{K_{fb}}$ when B_{vir} and K_{vir} were set as 0.83 Nms/rad and 25 Nm/rad, respectively

torque controller gain G_t. As the value of the torque controller gain G_t is increased from 20 rad/(sNm) to 30 rad/(sNm), the force required to move the brake pedal reduces from 1.49% to 0.91% of the 40 Nm torque output capability of the brake pedal. The experimental results in Fig. 8(*a*) align well with the analysis in Sec. 5, which demonstrates the positive influence of increasing torque controller gain G_t on null impedance rendering performance.

6.2.2 Spring Rendering Performance. The implementation of virtual constraints to restrict users from accessing undesired regions of the workspace is commonly achieved through spring rendering, making it a crucial control mode. The experimental verification of the spring rendering performance for two levels of desired virtual stiffness, with K_{ref} values of 50 Nm/rad and 100 Nm/rad, is presented in Fig. 8(*b*). To determine the rendered stiffness of the SDEA$_{K_{fb}}$ under VSIC, predetermined torques are applied to the end effector, and the resulting deflections are measured. A least-squares fit to the experimental data reveals that the values of K_{vir} are 49.63 Nm/rad with R^2 of 0.99 and 98.30 Nm/rad with R^2 of 0.99 with 0.73% and 0.25% the observed errors, respectively.

These experiments are also conducted with $G_t = 25$ rad/(sNm). The performance of spring rendering is evaluated for two levels of virtual stiffness: $K_{ref} = 50$ Nm/rad and 100 Nm/rad. A least-square fit to the experimental data reveals that for $K_{ref} = 50$ Nm/rad, the value of K_{vir} is 49.86 Nm/rad with $R^2 = 0.99$, resulting in an error of 1.48%. For $K_{ref} = 100$ Nm/rad, the value of K_{vir} is 97.88 Nm/rad with $R^2 = 0.99$, resulting in an error of 0.39%. These findings align with the analysis presented in Sec. 5, indicating the beneficial effect of increasing the torque controller gain G_t and desired virtual stiffness K_{ref} on the spring rendering performance.

Experiments were carried out to evaluate the system's ability to produce the proper virtual spring forces when the end effector is excited by dynamic human inputs during spring rendering using SDEA and SDEA$_{K_{fb}}$. Both systems were tested using a K_{ref} value of 50 Nm/rad, and the normalized root-mean-square error (NRMSE) values were recorded as 3.97% for SDEA and 5.09% for SDEA$_{K_{fb}}$, respectively. The experimental results align with the theoretical analysis, which predicts that the NRMSE of SDEA$_{K_{fb}}$ would be higher than that of SDEA due to the unmeasured B_f.

6.2.3 Voigt Model Rendering Performance. Figure 8(*c*) presents experimental verification of the Voigt model rendering performance of SDEA$_{K_{fb}}$. In this experiment, the end effector of the brake pedal was excited by an ideal velocity source imposing sine waves at eight distinct frequencies, ranging from 1 rad/s to 16 rad/s, while the brake pedal was rendering a Voigt model. The resulting interaction forces were recorded and presented as the Bode plot in Fig. 8(*c*). The average error between the experimental data and theoretical predictions in this Bode plot was computed as 4.5%, indicating high fidelity Voigt models rendering as predicted by theoretical results.

Experimental validation of the interaction performance of the SDEA$_{K_{fb}}$ brake pedal, rendering a Voigt model with $K_{ref} = 100$ Nm/rad and $B_{ref} = 0.01$ Nms/rad, under dynamic user inputs, was also conducted. Desired interaction torques derived from the Voigt model and the corresponding interaction torques measured using the series damped elastic element were compared. The resulting NRMSE of 1.1% confirms the accuracy of the rendering. A similar experiment was carried out for the SDEA brake pedal, yielding an NRMSE of 1%. As anticipated from the theoretical analysis, the higher NRMSE of SDEA$_{K_{fb}}$ compared to SDEA is attributed to the parasitic damping effect of the filter and the absence of damping on the computed force in the series elastic element.

7 Conclusion

We have established a fundamental rendering limitation for SEA when the inherent damping of the series elastic element is considered in the system model. We have proven that the viscous damping of the physical filter enables passive rendering of stiffness levels that are higher than the physical stiffness of the filter, as well as rendering Voigt models whose damping levels exceed that of the physical damping of the plant. This result has practical consequences, as SEA with an ideal series spring is an idealization, and every physical spring implementation possesses some level of dissipation. Furthermore, this result can guide practical designs of systems with SEA, as intentional utilization of larger physical damping levels in the series elastic element can extend the range of passively renderable virtual environments.

We have studied a widely used controller for SEA, where the forces induced on the series damping element are neglected in the feedback. Note that this model, called $\text{SDEA}_{K_{fb}}$ under VSIC, corresponds to the most common SEA controllers; however, our analysis considers the inherent damping of the series elastic element in the plant model. We have established necessary and sufficient conditions for the passivity of $\text{SDEA}_{K_{fb}}$ under VSIC during Voigt model, linear spring, and null impedance rendering. We have compared these results with the passivity conditions for S(D)EA under VSIC, to establish the effect of unmeasured series physical damping on the results. Our results provide the proper passivity bounds for a realistic model of SEA under VSIC.

We have derived passive physical equivalents of $\text{SDEA}_{K_{fb}}$ under VSIC while rendering Voigt, linear springs, and the null impedance models. The passive physical equivalents not only make the rendered impedance and parasitic dynamics of the closed-loop system explicit but also enable the objective comparisons among the S(D)EA models in terms of their rendering performance. Through the passive physical equivalents, we have rigorously compared the effects of measuring and omitting the damping force of the series elastic element on the closed-loop rendering performance of the system. We have shown that if the force acting on B_f is used in feedback control (SDEA under VSIC), this additional information has beneficial effects on haptic rendering performance, enabling direct control of damping during passive Voigt model renderings. On the other hand, if force on B_f is not used in feedback control ($\text{SDEA}_{K_{fb}}$ under VSIC), then B_f acts as an additive effect in addition to more indirectly controllable effective damping terms that can still be adjusted to passively render Voigt models.

We have also compared SDEA and $\text{SDEA}_{K_{fb}}$ under VSIC in terms of their effective impedances and shown that parasitic damping effects are higher for $\text{SDEA}_{K_{fb}}$. The maximum passively renderable virtual stiffness is limited by the physical stiffness of the filter for SDEA under VSIC [14,15,22], while [15] has proven that the unmeasured damping effect on the physical filter of $\text{SDEA}_{K_{fb}}$ can help exceed this physical spring stiffness bound. We have extended this analysis to Voigt model rendering without the assumption of positive controller gains, and studied the performance tradeoff through realizations.

Table 1 illustrates the realizations of the S(D)EA models under VSIC while rendering null impedance, springs, and Voigt models. It is important to note the continuity among these realizations. For example, the null impedance realization for SEA under VSIC can be obtained from the Voigt model realization for SDEA or $\text{SDEA}_{K_{fb}}$ by setting B_{ref}, K_{ref}, and B_f to zero.

Throughout the paper, proportional controllers are preferred to simplify the analysis while capturing the main effects of interest. Introducing more complex controllers significantly complicates realizations, making their interpretation much harder.

While the passivity conditions and physical realizations are informative, they also impose relatively conservative bounds to ensure the coupled stability of interactions. More relaxed coupled stability conditions can be established using less conservative analysis techniques, such as time domain passivity [39] or complementary stability [40–42]. However, these techniques depend on numerical calculations or optimizations; hence, they cannot offer closed-form analytical solutions and a general understanding of the tradeoffs.

Our future work involves extending the passive realizations to fractional order control systems [43,44], as interpretations of such controllers can significantly benefit from physical intuition.

Acknowledgment

Kenanoglu's work was carried out during his graduate studies at Sabanci University.

Funding Data

- TUBITAK (Grant Nos. 216M200 and 23AG003; Funder ID: 10.13039/501100004410).

Data Availability Statement

The datasets generated and supporting the findings of this article are obtainable from the corresponding author upon reasonable request.

Appendix A: Proof of Proposition 1

The proof of Proposition 1 can be presented as follows:

Since both the low- and high-frequency dynamics have a pole at the origin, $Z_{\text{SDEA}_{\text{cl}}}$ possesses a pole at the origin and with an equal number of remaining poles and zeros. The passivity of $Z_{\text{SDEA}_{\text{cl}}}$ implies that it can have no right-hand plane (RHP) poles or zeros. Furthermore, any complex imaginary poles are simple with positive real residues.

The following complex integral is considered $\oint [Z_{\text{SDEA}_{\text{cl}}}(s) - B_f]\, ds$ along the directed closed contour depicted in Fig. 9. Given that the contour includes infinitesimal indentations around the pole at the origin and possible (representative) simple complex poles on the imaginary axis, Cauchy's residue theorem ensures that the complex integral evaluates to zero, since the integrant is analytic everywhere along and inside the contour.

The contour can be divided into six parts: The semi-infinite negative (*I*) and positive (*II*) imaginary axes (depicted in black), the outer semicircle (*III*) at infinity (depicted in blue), and the infinitesimal semicircular indentation (*IV*) around the origin and representative infinitesimal semicircular indentations (*V*–*VI*) around a pair of simple complex conjugate poles (depicted in red).

Since $Z_{\text{SDEA}_{\text{cl}}}$ models the impedance of a physical system, the real part of this complex function is even, while the imaginary part is odd. Accordingly, for the complex the integrals taken along the negative

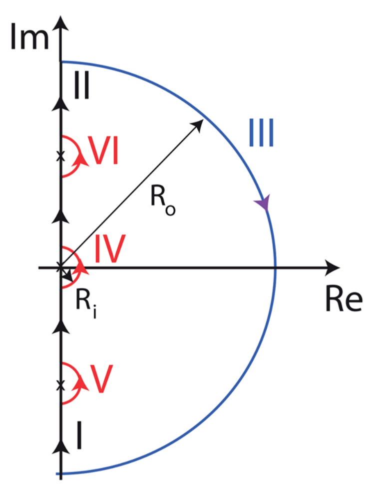

Fig. 9 The directed closed contour (with indentations around the simple poles) used for the complex integral

(I) and positive (II) axes, the imaginary parts cancel out, while the real parts are added to result in $\int_{I+II}\left[Z_{SDEA_{cl}}(s)-B_f\right]ds = 2i\int_0^\infty\left[\Re\{Z_{SDEA_{cl}}(\omega)\}-B_f\right]d\omega$.

Since $Z_{SDEA_{cl}}(s\to\infty)=\frac{K}{s}+B_f$, the integral taken along the outer semicircle at infinity evaluates to $\lim_{R_o\to\infty}\int_{III}\frac{K}{s}\,ds = \lim_{R_o\to\infty}\int_{\pi/2}^{-\pi/2}\frac{KiR_oe^{i\theta}}{R_oe^{i\theta}}d\theta = -i\pi K$.

Similarly, since $Z_{SDEA_{cl}}(s\to 0)=\frac{K_{vir}}{s}+B_{vir}$, the integral taken on the infinitesimal semicircle around zero evaluates to $\lim_{R_i\to 0}\int_{IV}\left[\frac{K_{vir}}{s}+(B_{vir}-B_f)\right]ds = \lim_{R_i\to 0}\int_{-\pi/2}^{\pi/2}\left[\frac{K_{vir}}{R_ie^{i\theta}}+(B_{vir}-B_f)\right] iR_ie^{i\theta}\,d\theta = i\pi K_{vir}$.

Finally, if simple complex poles exist, the infinitesimal semicircular indentations (V − VI) around these complex poles will contribute to the integral with a positive value $i\pi 2\Delta\geq 0$, due to their (equal) positive real residues Δ. Collecting all terms together and rearranging, one can express

$$\pi(K_{vir}-K)+2\pi\Delta+2\int_0^\infty\left[\Re\{Z_{SDEA_{cl}}(\omega)\}-B_f\right]d\omega = 0 \quad (A1)$$

The available bandwidth Ω_a of any causal system is defined as the finite frequency after which the closed-loop system converges to its plant dynamics [45]. In particular, $\Re\{Z_{SDEA_{cl}}(\omega)\}$ can be made arbitrarily close to B_f for $\omega>\Omega_a$ for all plants with SDEA for a sufficiently large (but finite) Ω_a.

Similarly, the performance bandwidth ω_p is defined as the frequency at which the virtual environment can be rendered as $Z_{SDEA_{cl}}(s)=\frac{K_{vir}}{s}+B_{vir}$. There exists a sufficiently small $\omega_p<\Omega_a$ for which the approximation error converges to zero.

Hence, the bounds in the definite integral of Eq. (A1) can be replaced with ω_p and Ω_a. Re-arranging, one can express

$$\int_{\omega_p}^{\Omega_a}\Re\{Z_{SDEA_{cl}}(\omega)\}d\omega+\pi\Delta = \frac{\pi}{2}(K-K_{vir})+\Omega_a B_f-\omega_p B_{vir} \quad (A2)$$

Passivity implies $\Re\{Z_{SDEA_{cl}}(\omega)\}\geq 0$ for all ω and $\Delta\geq 0$. Consequently, Eq. (A2) indicates that

$$\frac{\pi}{2}K+\Omega_a B_f\geq\frac{\pi}{2}K_{vir}+\omega_p B_{vir}$$

concluding the proof for all causal LTI controllers.

The result can be generalized to other causal controllers, including nonlinear and time-varying ones [46], since for an LTI plant, LTI controllers can achieve optimal performance. Consequently, for an LTI plant, optimal performance obtained by a causal stabilizing LTI controller determines the performance limits that cannot be improved by any other causal stabilizing controller. Accordingly, as long as the SDEA plant is LTI, the rendering limitation expressed in Eq. (A2) is valid for all casual controllers.

Appendix B: Proof of Proposition 2

The proof of Proposition 2 can be presented as follows:

According to the positive realness theorem [26,47],

- *$Z(s)$ has no poles in the right half plane:* If Routh–Hurwitz stability criterion is applied, there is no pole in the open right half plane for $Z_{Voigt}^{SDEA_{K_{fb}}}(s)$, since $(\alpha+1)$ is non-negative, and the inner motion control loop is asymptotically stable.
- *Any poles of Z(s) on the imaginary axis are simple with positive and real residues:* There exist no poles on the imaginary axis, except at $s=0$, as long as $(\alpha+1)$ is non-negative. For the pole at $s=0$, the residue equals to $\frac{\alpha}{\alpha+1}K_{ref}$, which should be positive. If $(\alpha+1)=0$, then the impedance transfer function has double poles at $s=0$, and the positive realness theorem is violated. Therefore, $(\alpha+1)=0$ violates passivity.
- $\mathrm{Re}[Z(jw)]\geq 0$ *for all w:* The sign of $\mathrm{Re}[Z_{Voigt}^{SDEA_{K_{fb}}}(jw)]$ can be checked by that of $H(jw)=d_6w^6+d_4w^4+d_2w^2$ with

$$d_2 = K\left(K(B_m+G_m+B_{ref}\alpha)+B_fK_{ref}\alpha\right)(\alpha+1) - KK_{ref}\alpha(B_f+B_m+G_m) \quad (B1)$$

$$d_4 = B_f(B_f+B_m+G_m)(B_m+G_m+B_{ref}\alpha) - J_m\alpha(K(B_{ref}+B_f)+B_fK_{ref}) \quad (B2)$$

$$d_6 = B_f J_m^2 \quad (B3)$$

Here, d_6 is positive, since B_f is positive. Condition (i) of Proposition 2 is imposed by the non-negative d_2. The last necessary and sufficient condition can be derived from $d_4\geq -2\sqrt{d_2d_6}$ [23] as Condition (vi) of Proposition 2, which is never satisfied when $B_{ref}=-\frac{B_m+G_m}{\alpha}$.

References

[1] Howard, R. D., 1990, "Joint and Actuator Design for Enhanced Stability in Robotic Force Control," Ph.D. thesis, MIT, Cambridge, MA.
[2] Pratt, G. A., and Williamson, M. M., 1995, "Series Elastic Actuators," IEEE/RSJ International Conference on Intelligent Robots and Systems, Pittsburgh, PA, Aug. 5–9, pp. 399–406.
[3] Robinson, D. W., Pratt, J. E., Paluska, D. J., and Pratt, G. A., 1999, "Series Elastic Actuator Development for a Biomimetic Walking Robot," IEEE International Conference on Advanced Intelligent Mechatronics, Atlanta, GA, Sept. 19–23, pp. 561–568.
[4] An, C., and Hollerbach, J., 1987, "Dynamic Stability Issues in Force Control of Manipulators," American Control Conference, Minneapolis, MN, June 10–12, pp. 821–827.
[5] Eppinger, S., and Seering, W., 1987, "Understanding Bandwidth Limitations in Robot Force Control," IEEE International Conference on Robotics and Automation, Raleigh, NC, Mar. 31–Apr. 3, pp. 904–909.
[6] Newman, W. S., 1992, "Stability and Performance Limits of Interaction Controllers," ASME J. Dyn. Syst., Meas., Control, **114**(4), pp. 563–570.
[7] Wyeth, G., 2008, "Demonstrating the Safety and Performance of a Velocity Sourced Series Elastic Actuator," IEEE International Conference on Robotics and Automation, Pasadena, CA, May 19–23, pp. 3642–3647.
[8] Otaran, A., Tokatli, O., and Patoglu, V., 2021, "Physical Human-Robot Interaction Using HandsOn-SEA: An Educational Robotic Platform With Series Elastic Actuation," IEEE Trans. Haptics, **14**(4), pp. 922–929.
[9] Vallery, H., Ekkelenkamp, R., Van Der Kooij, H., and Buss, M., 2007, "Passive and Accurate Torque Control of Series Elastic Actuators," IEEE/RSJ International Conference on Intelligent Robots and Systems, San Diego, CA, Oct. 29–Nov. 2, pp. 3534–3538.
[10] Vallery, H., Veneman, J., Van Asseldonk, E., Ekkelenkamp, R., Buss, M., and Van Der Kooij, H., 2008, "Compliant Actuation of Rehabilitation Robots," IEEE Rob. Autom. Mag., **15**(3), pp. 60–69.
[11] Tagliamonte, N. L., and Accoto, D., 2014, "Passivity Constraints for the Impedance Control of Series Elastic Actuators," Inst. Mech. Eng., Part I, **228**(3), pp. 138–153.
[12] Calanca, A., Muradore, R., and Fiorini, P., 2017, "Impedance Control of Series Elastic Actuators: Passivity and Acceleration-Based Control," Mechatronics, **47**, pp. 37–48.
[13] Tosun, F. E., and Patoglu, V., 2020, "Necessary and Sufficient Conditions for the Passivity of Impedance Rendering With Velocity-Sourced Series Elastic Actuation," IEEE Trans. Rob., **36**(3), pp. 757–772.
[14] Kenanoglu, C. U., and Patoglu, V., 2024, "Passive Realizations of Series Elastic Actuation: Effects of Plant and Controller Dynamics on Haptic Rendering Performance," IEEE Trans. Haptics, **17**(4), pp. 882–899.
[15] Kenanoglu, C. U., and Patoglu, V., 2023, "A Fundamental Limitation of Passive Spring Rendering With Series Elastic Actuation," IEEE Trans. Haptics, **16**(4), pp. 456–462.
[16] Kenanoglu, C. U., and Patoglu, V., 2022, "Passivity of Series Elastic Actuation Under Model Reference Force Control During Null Impedance Rendering," IEEE Trans. Haptics, **15**(1), pp. 51–56.
[17] Hurst, J., Rizzi, A., and Hobbelen, D., 2004, "Series Elastic Actuation: Potential and Pitfalls," International Conference on Climbing and Walking Robots, pp. 1–6.
[18] Oblak, J., and Matjačić, Z., 2011, "Design of a Series Visco-Elastic Actuator for Multi-Purpose Rehabilitation Haptic Device," J. Neuroeng. Rehabil., **8**(1), pp. 1–14.
[19] Garcia, E., Arevalo, J. C., Muñoz, G., and Gonzalez-de Santos, P., 2011, "Combining Series Elastic Actuation and Magneto-Rheological Damping for the Control of Agile Locomotion," Rob. Auton. Syst., **59**(10), pp. 827–839.
[20] Laffranchi, M., Tsagarakis, N., and Caldwell, D. G., 2011, "A Compact Compliant Actuator With Variable Physical Damping," IEEE International Conference on Robotics and Automation, Shanghai, China, May 9–13, pp. 4644–4650.
[21] Kim, M. J., Werner, A., Loeffl, F. C., and Ott, C., 2017, "Enhancing Joint Torque Control of Series Elastic Actuators With Physical Damping," IEEE International Conference on Robotics and Automation (ICRA), Singapore, May 29–June 3, pp. 1227–1234.

[22] Mengilli, U., Orhan, Z. O., Caliskan, U., and Patoglu, V., 2021, "Passivity of Series Damped Elastic Actuation Under Velocity-Sourced Impedance Control," IEEE World Haptics Conference (WHC), Montreal, QC, Canada, July 6–9, pp. 379–384.
[23] Mengilli, U., Caliskan, U., Orhan, Z. O., and Patoglu, V., 2020, "Two-Port Analysis of Stability and Transparency in Series Damped Elastic Actuation," arXiv:2011.00664.
[24] Focchi, M., Medrano-Cerda, G. A., Boaventura, T., Frigerio, M., Semini, C., Buchli, J., and Caldwell, D. G., 2016, "Robot Impedance Control and Passivity Analysis With Inner Torque and Velocity Feedback Loops," Control Theory Technol., **14**(2), pp. 97–112.
[25] Kenanoglu, O. T., Kenanoglu, C. U., and Patoglu, V., 2023, "Effect of Low-Pass Filtering on Passivity and Rendering Performance of Series Elastic Actuation," IEEE Trans. Haptics, **16**(4), pp. 567–573.
[26] Colgate, J. E., and Hogan, N., 1988, "Robust Control of Dynamically Interacting Systems," Int. J. Control, **48**(1), pp. 65–88.
[27] Colgate, E., and Hogan, N., 1989, "An Analysis of Contact Instability in Terms of Passive Physical Equivalents," Proceedings of International Conference on Robotics and Automation, Scottsdale, AZ, May 14–19, pp. 404–409.
[28] Smith, M. C., 2002, "Synthesis of Mechanical Networks: The Inerter," IEEE Trans. Autom. Control, **47**(10), pp. 1648–1662.
[29] Chen, M. Z., and Smith, M. C., 2007, "Mechanical Networks Comprising One Damper and One Inerter," IEEE European Control Conference (ECC), Kos, Greece, July 2–5, pp. 4917–4924.
[30] Chen, M. Z., and Smith, M. C., 2009, "Restricted Complexity Network Realizations for Passive Mechanical Control," IEEE Trans. Autom. Control, **54**(10), pp. 2290–2301.
[31] Chen, M. Z., Wang, K., Zou, Y., and Lam, J., 2012, "Realization of a Special Class of Admittances With One Damper and One Inerter," IEEE Conference on Decision and Control (CDC), Maui, HI, Dec. 10–13, pp. 3845–3850.
[32] Chen, M. Z., Wang, K., Zou, Y., and Lam, J., 2013, "Realization of a Special Class of Admittances With One Damper and One Inerter for Mechanical Control," IEEE Trans. Autom. Control, **58**(7), pp. 1841–1846.
[33] Chen, M. Z., Wang, K., Shu, Z., and Li, C., 2013, "Realizations of a Special Class of Admittances With Strictly Lower Complexity Than Canonical Forms," IEEE Trans. Circuits Syst. I, **60**(9), pp. 2465–2473.
[34] Chen, M. Z., Wang, K., Zou, Y., and Chen, G., 2015, "Realization of Three-Port Spring Networks With Inerter for Effective Mechanical Control," IEEE Trans. Autom. Control, **60**(10), pp. 2722–2727.
[35] Caliskan, U., Apaydin, A., Otaran, A., and Patoglu, V., 2018, "A Series Elastic Brake Pedal to Preserve Conventional Pedal Feel Under Regenerative Braking," IEEE/RSJ International Conference on Intelligent Robots and Systems (IROS), Madrid, Spain, Oct. 1–5, pp. 1367–1373.
[36] Caliskan, U., and Patoglu, V., 2020, "Efficacy of Haptic Pedal Feel Compensation on Driving With Regenerative Braking," IEEE Trans. Haptics, **13**(1), pp. 175–182.
[37] Colgate, J. E., 1988, "The Control of Dynamically Interacting Systems," Ph.D. thesis, Massachusetts Institute of Technology, Cambridge, MA.
[38] Losey, D. P., and O'Malley, M. K., 2017, "Effects of Discretization on the K-Width of Series Elastic Actuators," IEEE International Conference on Robotics and Automation (ICRA), Singapore, May 29–June 3, pp. 421–426.
[39] Hannaford, B., and Ryu, J.-H., 2002, "Time Domain Passivity Control of Haptic Interfaces," IEEE Trans. Rob. Autom., **18**(1), pp. 1–10.
[40] Buerger, S. P., and Hogan, N., 2007, "Complementary Stability and Loop Shaping for Improved Human–Robot Interaction," IEEE Trans. Rob., **23**(2), pp. 232–244.
[41] Aydin, Y., Tokatli, O., Patoglu, V., and Basdogan, C., 2018, "Stable Physical Human-Robot Interaction Using Fractional Order Admittance Control," IEEE Trans. Haptics, **11**(3), pp. 464–475.
[42] Aydin, Y., Tokatli, O., Patoglu, V., and Basdogan, C., 2020, "A Computational Multicriteria Optimization Approach to Controller Design for Physical Human-Robot Interaction," IEEE Trans. Rob., **36**(6), pp. 1791–1804.
[43] Tokatli, O., and Patoglu, V., 2015, "Stability of Haptic Systems With Fractional Order Controllers," IEEE/RSJ International Conference on Intelligent Robots and Systems (IROS), Hamburg, Germany, Sept. 28–Oct. 2, pp. 1172–1177.
[44] Tokatli, O., and Patoglu, V., 2018, "Using Fractional Order Elements for Haptic Rendering," Robotics Research, Springer, Cham, Switzerland, pp. 373–388.
[45] Stein, G., 2003, "Respect the Unstable," IEEE Control Syst. Mag., **23**(4), pp. 12–25.
[46] Chen, J., Fang, S., and Ishii, H., 2019, "Fundamental Limitations and Intrinsic Limits of Feedback: An Overview in an Information Age," Annu. Rev. Control, **47**, pp. 155–177.
[47] Haykin, S., 1970, *Active Network Theory*, Addison-Wesley Pub. Co, Reading, MA.